

Supporting Information for:

Observing imperfection in atomic interfaces for van der Waals heterostructures

Aidan. P. Rooney¹, Aleksey Kozikov^{2,3,4}, Alexander N. Rudenko⁵, Eric Prestat¹, Matthew J Hamer^{2,3,4}, Freddie Withers⁶, Yang Cao^{2,3,4}, Kostya S. Novoselov^{2,3,4}, Mikhail I. Katsnelson⁵, Roman Gorbachev^{2,3,4} Sarah J. Haigh^{1,4*}*

1. School of Materials, University of Manchester, Manchester M13 9PL, UK
2. Manchester Centre for Mesoscience and Nanotechnology, University of Manchester, Manchester M13 9PL, UK
3. School of Physics and Astronomy, University of Manchester, Oxford Road, Manchester, M13 9PL, UK
4. National Graphene Institute, University of Manchester, Manchester M13 9PL, UK
5. Institute for Molecules and Materials, Radboud University, 6525 AJ Nijmegen, Netherlands
6. College of Engineering, Mathematics and Physical Sciences, University of Exeter, Exeter, Devon, EX4 4SB, UK

1. Density functional theory calculations

The experimental HAADF STEM images were compared to density functional theory (DFT) calculations in order to help explain the observed structures.

DFT calculations were carried out using the projected augmented-wave method (PAW)¹ as implemented in the Vienna ab initio simulation package (VASP)^{2,3}. Exchange and correlation effects were taken into account within the dispersion-corrected nonlocal vdW-DF functional⁴ in the parametrization of Klimeš *et al.* (optB88-vdW)⁵, which shows good performance for weakly-bonded layered solids including graphene and h-BN⁶. An energy cutoff of 550 eV for the plane-wave basis and the convergence threshold of 10^{-6} eV were used in the self-consistent solution of the Kohn-Sham equations, which have proven to be sufficient to obtain numerically converged forces to within 10^{-2} eV/Å. For the 2nd (3rd) row transition metals (TMs) the 5s and 4d (6s and 5d) electrons only were treated as valent. The inclusion of the 4p (5p) electrons did not affect the interlayer separations by more than 0.01 Å. For the p-elements, only s and p electrons of the outer shell were treated as valent. The encapsulated systems were modelled in the bulk geometry with the unit cell containing one or two layers of TMDC and three layers of hBN in the AA' stacking. The atomic structure and lattice parameters were fully relaxed. To minimize the lattice mismatch between the hBN and TMDC down to approximately 1% (see Table S1) we use hexagonal unit cells with the following lattice parameters for MoS₂, WS₂, NbSe₂, MoSe₂, and WSe₂, respectively: 5a, 5a, 7a, 8a, 8a, where $a \sim 2.50$ Å is the lattice parameter of h-BN. The Brillouin zone was sampled by a uniform distribution of 64 or 16 **k**-points, depending on the unit cell dimensions.

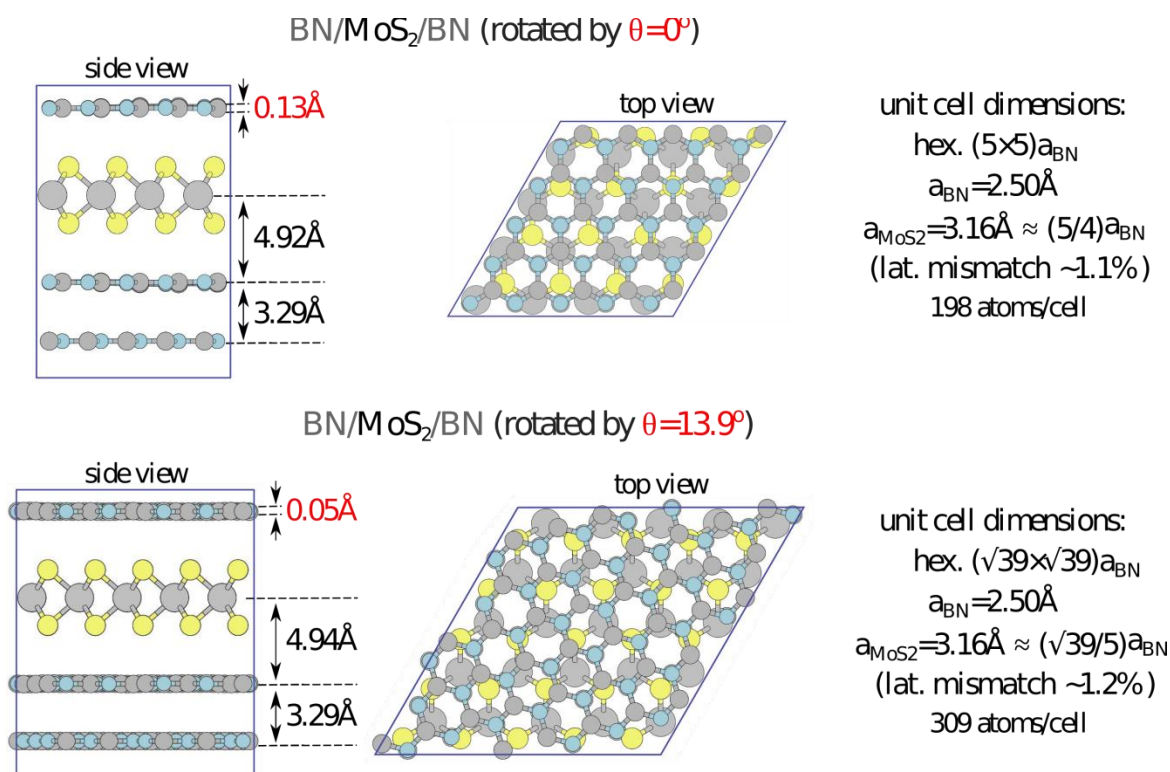


Figure S1. Effect of twist angle on interlayer separation in hBN/MoS₂/hBN. **Top:** Side and top views of hBN encapsulated MoS₂ with a twist angle of 0.0°. **Bottom:** Side and top views of hBN encapsulated MoS₂ with a twist angle of 13.9°. Both fully relaxed structures show negligible differences in interlayer separation, hBN spacing and variation.

In order to assess the accuracy of the DFT calculations and reduce the number of computationally expensive simulations to be run, the effect of lattice twist angle on distances in the heterostructure system was investigated. A monolayer of MoS₂ encapsulated in hBN was orientated with azimuthal twist angles of 0° and 13.9° and both systems relaxed (see Fig. S1). The bulk spacing of hBN, the interlayer separation between MoS₂ and hBN, and the variation in hBN vertical positions differed by $\leq 0.08 \text{ \AA}$, which is significantly less than the accuracy of our experimental data ($\pm 0.5 \text{ \AA}$). Therefore, we assume the effect of twist angle on the measured distances of our system is negligible.

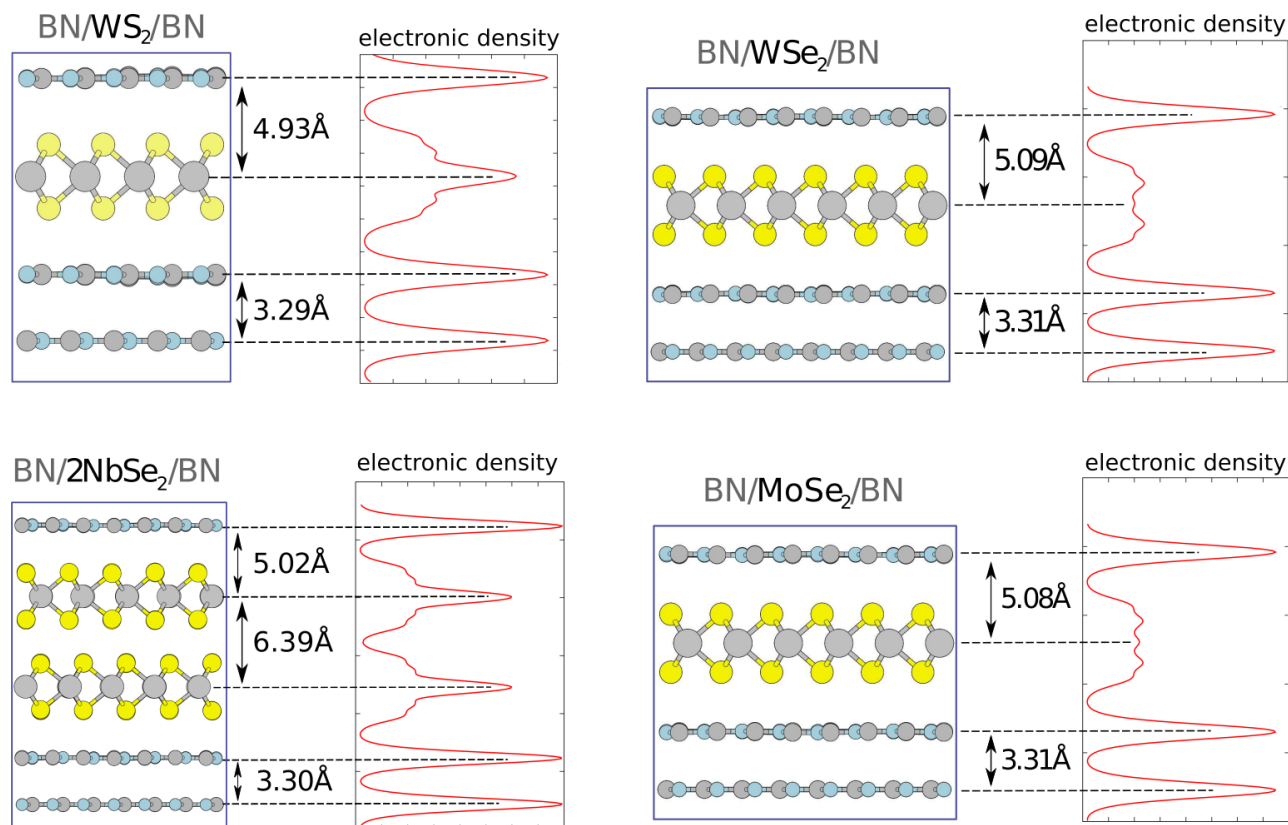


Figure S2. Interlayer separation in hBN/TMDC/hBN systems as predicted by DFT. WS₂, MoSe₂ and WSe₂ monolayers and NbSe₂ bilayer flakes trapped in hBN. Important distances are annotated on each system. All interlayer distances are predicted to be between 4.92 – 5.09 Å.

The calculation parameters used for the hBN/MoS₂/hBN system were applied to monolayer and bilayer TMDC systems with twist angles of 0°. Between all systems the bulk hBN spacing varies by 0.02 Å, whilst the interlayer distances lie between 4.92 – 5.09 Å. These values do not explain the discrepancies observed in our experimental results, leading us to question whether differences in chemical reactivity can explain why MoSe₂ and WSe₂ deviate from the expected values. Table S2 shows DFT calculated values for the work function and electron affinity for each TMDC. The energy terms used to calculate these properties are E_{VBM} and E_{cbm} ,

corresponding to the valence band and conduction band minima, and E_{vac} corresponding to vacuum. Low values of work function predict a higher reactivity with acceptor species (behaves as a nucleophile), whilst high values of electron affinity predict a higher reactivity with donor species (behaves as an electrophile). From this we would expect MoSe₂ and WSe₂ to be the most nucleophilic TMDCs, however the values are not extreme enough to warrant prediction of substantial reaction with contaminant species trapped between the layers.

Table S1: Lattice mismatches ($\Delta a = (a_{exp} - a_{TMDC})/a_{TMDC}$) between the experimental TMDC lattice constants (a_{exp}) and lattice constants used for DFT simulations of BN/TMDC/BN heterostructures (a_{TMDC}). Experimental TMDC lattice constants are taken from Ref. 7. N_{at} is the number of atoms in the simulated supercell.

TMDC	a_{TMDC}/a_{BN}	$a_{exp}, \text{\AA}$	$\Delta a, \%$	N_{at}
MoS ₂	5/4	3.16	+1.1	198
MoS ₂ *	$\sqrt{39}/5$	3.16	+1.2	309
WS ₂	7/5	3.15	+0.8	198
NbSe ₂	7/5	3.44	-1.7	444
MoSe ₂	8/6	3.29	-1.3	492
WSe ₂	8/6	3.28	-1.6	492

* Rotated by 13.9°

Table S2
Quantities related to the reactivity of TMDC: work function and electron affinity

	MoS ₂	WS ₂	MoSe ₂	WSe ₂	NbSe ₂
Work function* = $E_{\text{VBM}} - E_{\text{vac}}$	5.93 eV	5.70 eV	5.33 eV	5.10 eV	5.55 eV
Electron affinity** = $E_{\text{CBM}} - E_{\text{vac}}$	4.27 eV	3.94 eV	3.88 eV	3.56 eV	5.55 eV

* lower values mean higher reactivity wrt acceptor species (like O₂)

** higher values mean higher reactivity wrt donor species (like metals)

Simulating defects at the interface

To better understand the extent to which an impurity may disrupt the interfaces for a van der Waals heterostructure, an OH molecule was added to the van der Waals gap between the upper hBN and the encapsulated monolayer WSe₂ as shown in Figure S3 below. The calculation was run identically to those presented in Figure S2 with the exception of the added impurity.

We find the separation of the upper hBN from the WSe₂ monolayer increases by 0.68 Å to 5.77 Å (5.09 Å in the pristine case) when an OH impurity is placed at the interface. In addition the separation of the lower hBN from the WSe₂ monolayer decreases slightly (to 4.97 Å). This theoretical result compares well to our measurement in the main text of 6.01 Å ± 0.56 Å. Nevertheless, limitations on the size of the simulation that can be performed and the use of periodic boundary conditions prevent us from modelling corrugations to the monolayers or

accurately reproducing the low defect densities we observe experimentally. As a result this comparison is qualitative at best.

It should be noted that previous DFT calculations have similarly predicted an increase in interlayer separation between graphene and silicon when the interface is perturbed by hydrogen or water impurities^{8,9}, and for chemisorbed oxygen on various TMDCs the oxygen-metal distances were found to be in the range of 2 Å¹⁰.

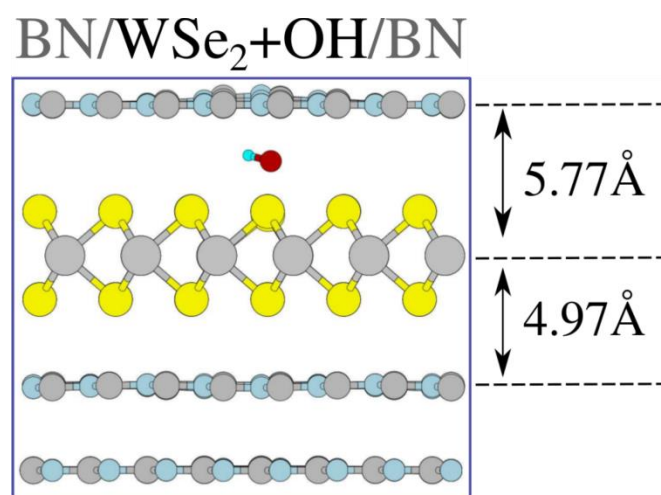


Figure S3. Interlayer separation in hBN/ WSe₂ + OH/ hBN systems as predicted by DFT. Important distances are annotated. The interlayer distance is increased from the pristine case by 0.68 Å to 5.77 Å, whilst the unperturbed side is decreased to 4.97 Å.

2. HAADF STEM image processing using principle component analysis

To accurately determine the lateral positions of the different 2D crystals layered within a van der Waals heterostructure, the high angle annular dark field (HAADF) scanning transmission electron microscopy (STEM) image needs to be carefully processed. Fig. S4A shows an atomic schematic of the structure being imaged in Fig. S4C (this image was first aligned using hBN fringes to remove scan noise and specimen drift artefacts). To quantitatively measure the interlayer spacing between two dissimilar crystals (hBN – TMDC) an intensity profile is acquired perpendicular to the lattice fringes, each profile having a width of one pixel (0.4 Å). A typical intensity profile taken from the raw image is shown in Fig. S4D, revealing that, although the peaks are visible, the exact positions of their maxima are not readily determined.

Principle component analysis (PCA) is a statistical algorithm which can be used to separate the components of a dataset by their degree of variability.¹¹ By assigning the axis parallel to the basal planes as the navigation axis, and the axis perpendicular to the basal planes (i.e. the direction of the intensity profile) as the signal axis, PCA can distinguish the components which comprise the raw intensity profile by their variance. A scree plot showing the explained variance ratio of each of principle component of the raw image is presented in Fig. S4B. As might be expected the components with the largest variation correspond to the main features in the image: in this case the peaks and troughs of the atomic planes in the heterostructure, whilst the components with the smallest variation are composed entirely of noise. Components between these two extremes hold some useful signal and some noise signal. As such, a judgement is made as to how many components to include in the reconstructed image; in this scenario we have chosen 21 components. Fig. S4E shows the reconstructed image, which compares favorably to

the original. The processed intensity profile in Fig. S4F now shows smooth peaks with readily identifiable maxima. This allows measurement of the distance between nearest neighbor fringes from these maxima with high precision. A peak finding algorithm¹², searching for local maxima can then be successfully applied to accurately identify the position of lattice planes.

Applying PCA to uniform structures shown in this work is very useful for denoising images and intensity profiles, however we note that it may prove to be a key method for analyzing images showing tortuous interfaces or heterogeneous features.

It should also be noted the different crystal lattices are azimuthally rotated to one another (sometimes referred to as ‘twist angle’). The lamella can be rotated such that each crystal comes ‘on zone’ and atomic resolution is observed from orientated lattices, as shown in Figure S5. This is accompanied by enhanced channeling contrast which can interfere with measurement accuracy. Therefore, to get equivalent signals from all lattices the lamellae were tilted to an angle where channeling contrast was minimized and the basal planes were aligned to the incident electron probe. This improved the success of the automated peak-finding and the accuracy of the interlayer separation measurement. The measured interlayer separations for different thicknesses and fabrication methods for WSe₂/hBN are presented in Table S3.

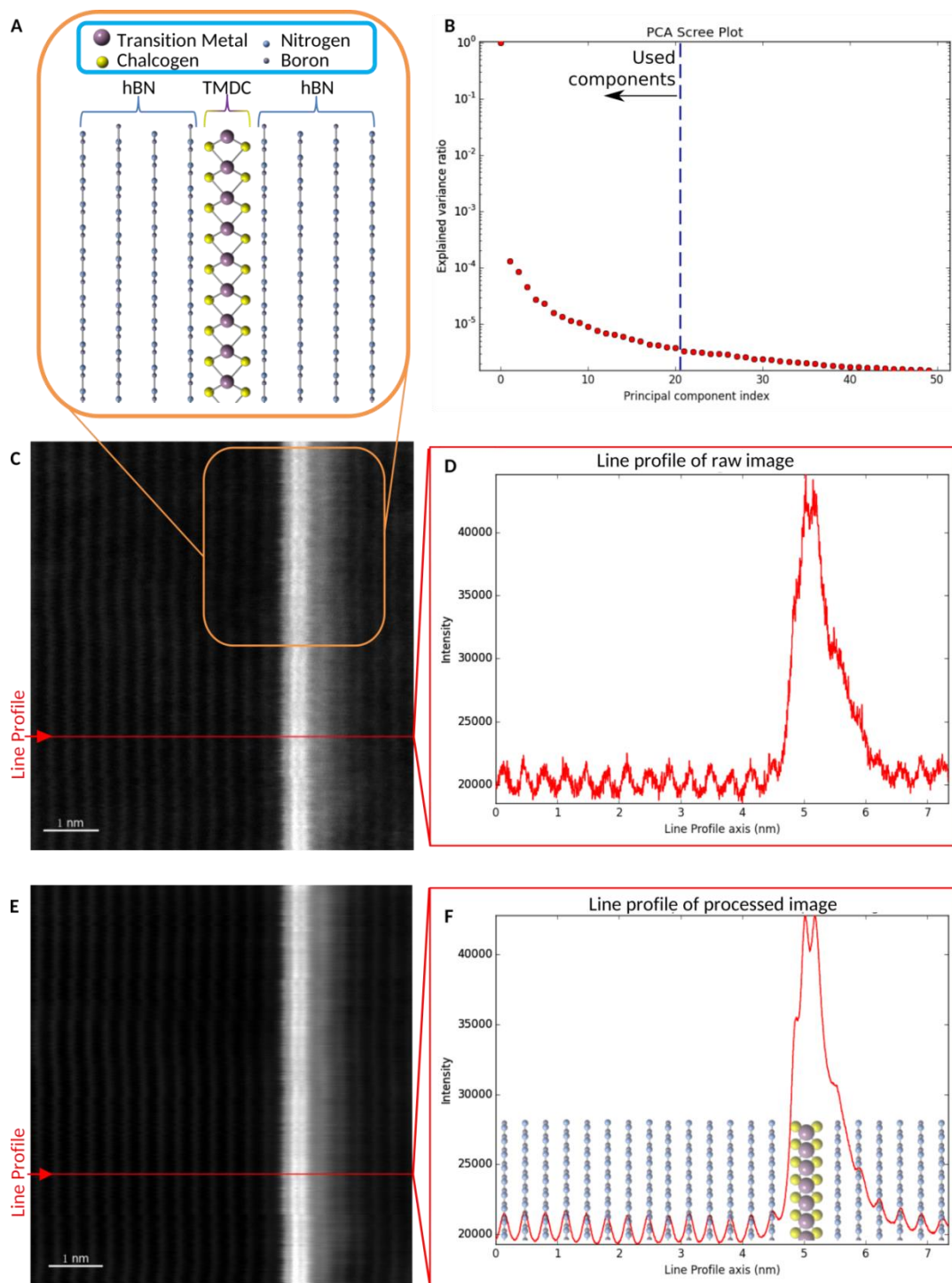


Figure S4. Denoising similar intensity profiles in HAADF STEM images. **A**, Schematic showing the positions of atoms in the highlighted region shown in **C**. A monolayer TMDC is encapsulated by bulk hBN. An example intensity profile **D** shows how noise prevents us from successfully identifying peaks which correspond to atomic positions. **B** The explained variance ratio of each component, with the threshold annotated. **E** The denoised image shows all the same features of its parent in **C**, however the intensity profile in **F** is now fully denoised and we can assign atomic components to each peak.

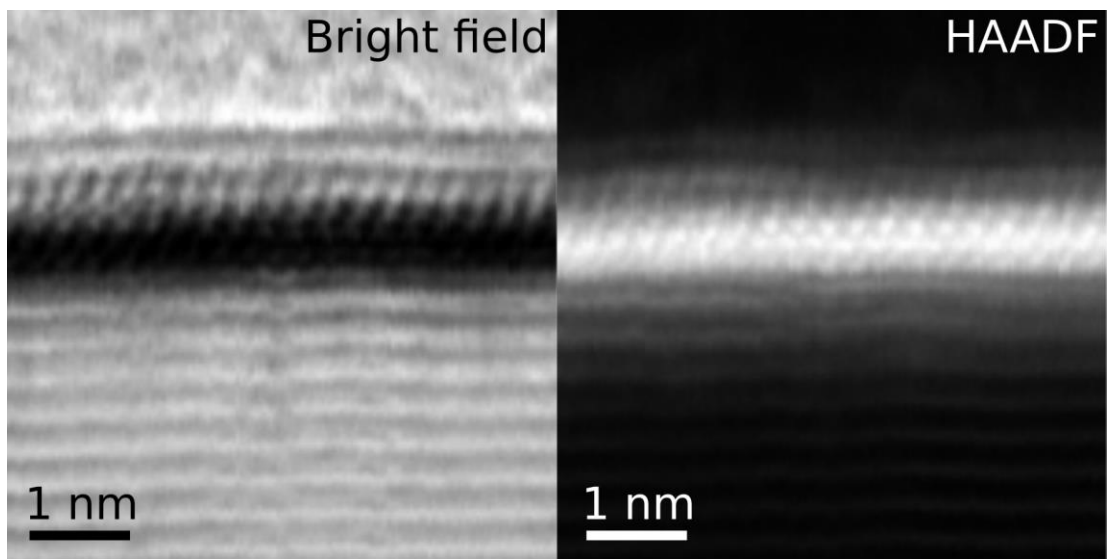


Figure S5. Left Bright field and Right HAADF STEM images of the same region. In this case the WSe_2 monolayer is aligned to the incident probe and the three rows of atomic columns (Se – W – Se) are resolved. Due to random azimuthal rotation of the encapsulating hBN they are not on zone and are seen instead as continual planes of atoms. For all other images considered in this work, the lamellae were tilted to this off-zone condition to give more accurate measurements and avoid dominant channeling contrast.

Table S3: Table of measured interlayer separations for 1-5L and bulk WSe_2 .

Thickness of WSe_2	Mean hBN – W distance (Å)	Standard Deviation (Å)
Monolayer	6.01	0.56
Bilayer	6.24	0.49
Trilayer	6.62	0.34
Four layer	6.61	0.41
Five layer	6.95	0.38
Bulk – Air	6.76	0.23
Bulk - Glovebox	5.51	0.20

Roughness analysis of buried interfaces

The perturbation of the van der Waals interface can be further quantified by measuring the roughness of the TMDC lattice fringe(s) relative to the nearest neighbor hBN fringe. This is captured as variation in the measurement of interlayer separation together with measurement error. This can be seen in the example datasets from 1-5 layer and bulk WSe₂ are presented in Fig. S6.

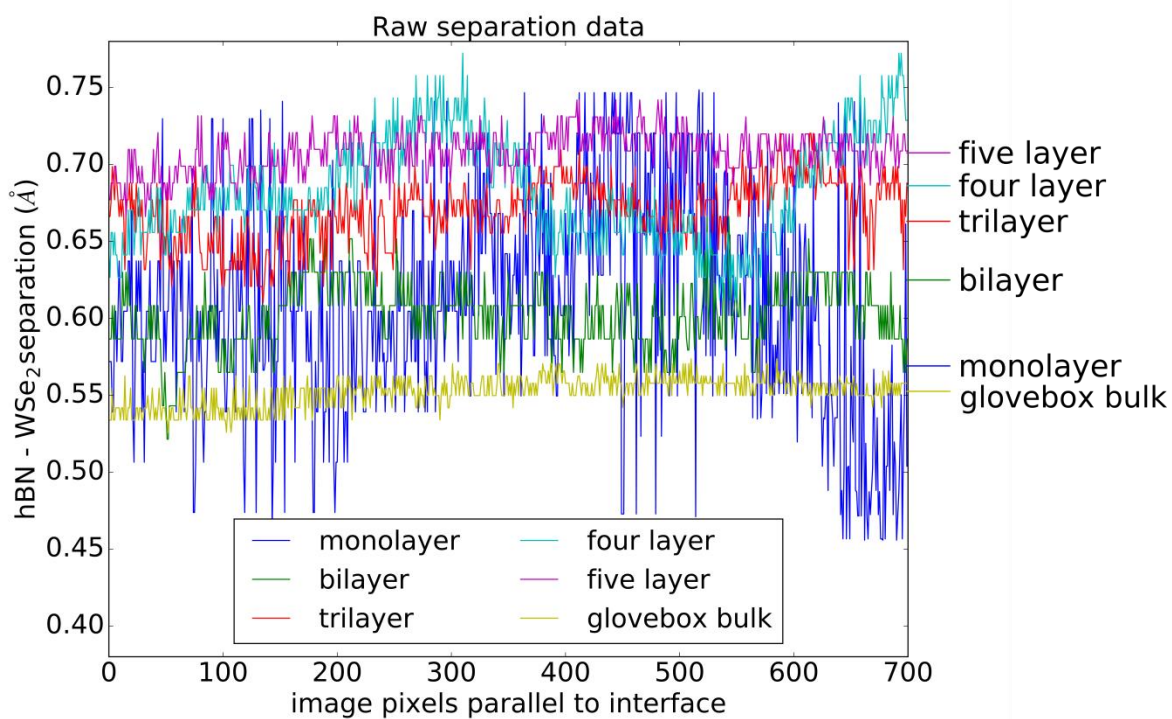


Figure S6. Unprocessed separation measurement data for different thicknesses of WSe₂.

The roughness average for 1-5 layer and glovebox fabricated bulk WSe₂ is plotted in Fig. S7.

The roughness was found using the roughness average (R_a):

$$R_a = \frac{1}{L} \int_0^L |Z(x)| dx$$

Where L is the distance over which the measurement (10 – 15 nm) was carried out and Z is the height at position x. As expected, thin flakes of WSe₂ are rougher than thicker flakes as the materials become stiffer with thickness.

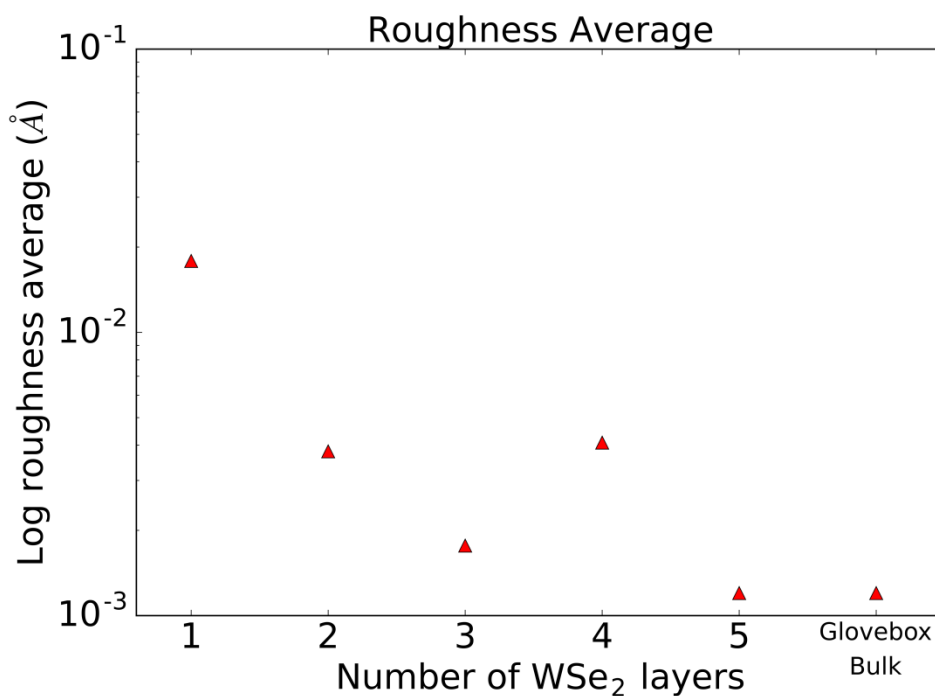


Figure S7. A log-plot of roughness average calculated from the separation measurements of 1-5 layer and glovebox bulk WSe₂. The thinner flakes show enhanced roughness as they deform around defects at the interface with hBN. Thicker flakes are stiffer and so less rough.

3. Spectrum imaging of WSe₂ heterostructures

Energy dispersive X-ray spectroscopy (EDXS) and electron energy loss spectroscopy (EELS) analysis was used to characterize the chemistry of the buried interfaces in WSe₂. The main motivation for this was to determine if the interfaces between WSe₂ and hBN had been chemically modified, resulting in an increased interlayer separation at this interface. Fig S8 shows the distribution of elements through the depth of the structure. Tungsten, selenium and nitrogen distributions confirm the successful encapsulation of the WSe₂. The background subtracted EELS carbon and nitrogen K-edge intensities plotted across the same region can be used to determine if contamination is present at these two interfaces either side of the WSe₂ monolayer. The carbon distribution clearly identifies the thick amorphous carbon coating on the surface of the upper hBN. The interfaces, in contrast, show no discernible presence of carbon. Similarly, oxygen shows no signal at the interfaces, only a small enhancement at the surface of the upper hBN. From this we conclude that any chemical modification of the WSe₂ is at a level below the detection limit of this technique (~1 at%).

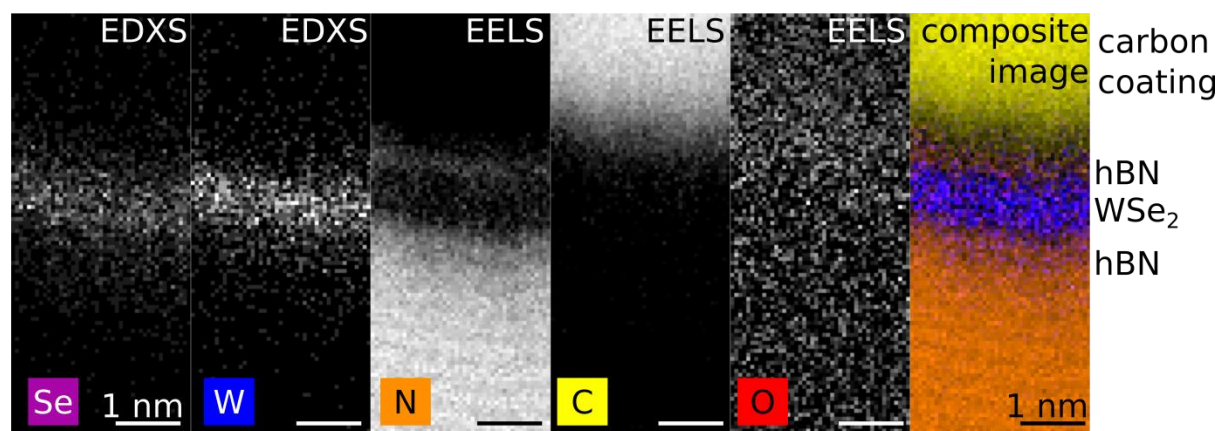


Figure S8. EDXS and EELS spectrum imaging, mapping the distribution of selenium, tungsten, nitrogen and carbon in a WSe_2 monolayer encapsulated in hBN. EDXS maps are formed from expressing the peak intensities as greyscale values for every pixel in the spectrum image. Maps for the selenium K- α and tungsten L- α characteristic X-ray peaks are shown leftmost. EELS maps are formed from plotting the intensities of background subtracted characteristic edges. The nitrogen, carbon and oxygen K-edges are plotted center. Rightmost is the composite image of all four maps, with selenium plotted magenta, tungsten purple, nitrogen orange, carbon yellow. No carbon or oxygen is seen in the interfaces between hBN and WSe_2 , despite the presence of an amorphous carbon coating on the surface of the structure to aid electron microscope sample preparation. The apparent bending of the basal planes is due to specimen drift during the long acquisition time used to maximize sensitivity. All scale bars 1 nm.

References

- (1) Blöchl, P. E. *Phys. Rev. B* **1994**, *50* (24), 17953–17979.
- (2) Kresse, G.; Furthmüller, J. *Phys. Rev. B* **1996**, *54* (16), 11169–11186.
- (3) Kresse, G.; Joubert, D. *Phys. Rev. B* **1999**, *59* (3), 1758–1775.
- (4) Dion, M.; Rydberg, H.; Schröder, E.; Langreth, D. C.; Lundqvist, B. I. *Phys. Rev. Lett.* **2004**, *92* (24), 246401.
- (5) Klimeš, J.; Bowler, D. R.; Michaelides, A. *J. Phys. Condens. Matter* **2010**, *22* (2), 022201.
- (6) Graziano, G.; Klimeš, J.; Fernandez-Alonso, F.; Michaelides, A. *J. Phys. Condens. Matter* **2012**, *24* (42), 424216.
- (7) Björkman, T. *J. Chem. Phys.* **2014**, *141* (7), 074708.
- (8) Wehling, T. O.; Lichtenstein, A. I.; Katsnelson, M. I. *Appl. Phys. Lett.* **2008**, *93* (20), 202110.
- (9) Rudenko, A. N.; Keil, F. J.; Katsnelson, M. I.; Lichtenstein, A. I. *Phys. Rev. B* **2011**, *84* (8), 085438.
- (10) Liu, H.; Han, N.; Zhao, J. *RSC Adv* **2015**, *5* (23), 17572–17581.
- (11) Peña, F. de la; iygr; Ben; Walls, M.; Sarahan, M.; Caron, J.; Garmannslund, A.; Ostasevicius, T.; Petras; Mazzucco, S.; Eljarrat, A.; Burdet, P.; Prestat, E.; Taillon, J.; Donval, G.; Johnstone, D.; Fauske, V. T.; MacArthur, K. E.; Nord, M.; Furnival, T.; Zagonel, L. F.; Aarholt, T. *hyperspy: HyperSpy 0.8.5*; 2016.
- (12) Oliphant, T. E. *Comput. Sci. Eng.* **2007**, *9* (3), 10–20.